nature portfolio

https://doi.org/10.1038/s41566-021-00820-z

Supplementary information

Room-temperature polaritonic non-Hermitian system with single microcavity

In the format provided by the authors and unedited

Supplementary information

Room-temperature polaritonic non-Hermitian system with single microcavity

Hyun Gyu Song, Minho Choi, Kie Young Woo, Chung Hyun Park, and Yong-Hoon Cho*

Department of Physics and KI for the NanoCentury, Korea Advanced Institute of Science and Technology (KAIST), 291 Daehak-ro, Yuseong-gu, Daejeon 34141, Republic of Korea

Tel.: +82-42-350-2589

*Corresponding author E-mail: yhc@kaist.ac.kr

Supplementary Text

Section 1. Identification of six-fold symmetry

Although the selective area growth method for hexagonal microwires can attain a certain degree of hexagonal geometry owing to the predetermined growth region (opening hole pattern), it cannot ensure six-fold symmetry. Because Wurtzite crystal structures intrinsically obtain the m-plane as the stable facet, the angle between adjacent planes is always 120°; this results in a hexagonal geometry. If the growth rate of each plane is anisotropic, it induces diverse hexagonal geometries, such as elongated geometry and asymmetry, which lead to a different length for each plane. The six-fold symmetry is generated exclusively under the condition of the isotropic growth rate of each plane. To observe the properties of diverse hexagonal geometries directly and obtain the degeneracy of tri↑-WGMs and tri↓-WGMs through the aspect of PL spectra, the freestanding condition is an essential factor. For this reason, we intentionally dispersed hexagonal microwires on a quartz substrate ($n \approx 1.4$) polished by sandpaper to reduce the effective refractive index while maintaining the total internal reflection (Fig. S1a). Fig. S1b-d represents PL spectra to investigate the correlation between WGMs and hexagonal geometries. Because the six-fold symmetry ensures hex-WGMs as well as tri↑-WGMs and tri↓-WGMs with degenerate eigenenergies, the PL spectrum appears to have double mode peaks compared to other geometrical aspects (Fig. S1b). Here, the optical path length of tri-WGMs and hex-WGMs is 4.5 R and 5.2 R, respectively, in the criterion of the circumradius (R) of the hexagonal geometry. In the elongated geometry, hex-WGMs cannot dwell a long time owing to the electric field distribution located near the edges[1]. Simultaneously, tri↑-WGMs and tri↓-WGMs with the same eigenenergy can be rigidly maintained in the cavity (Fig. S1c). In asymmetrical geometry, hex-WGMs cannot be generated because of the destruction of the symmetry. Although tri-WGMs can be formed in this asymmetrical geometry, the small optical path length difference between tri↑-WGMs and tri↓-WGMs causes degeneracy lifting; therefore, the PL spectrum of the asymmetrical geometry obtains twin peaks (Fig. S1d). This geometry cannot be utilized to generate coupled tri-polariton pairs between tri↑- and tri↓-WGMs.

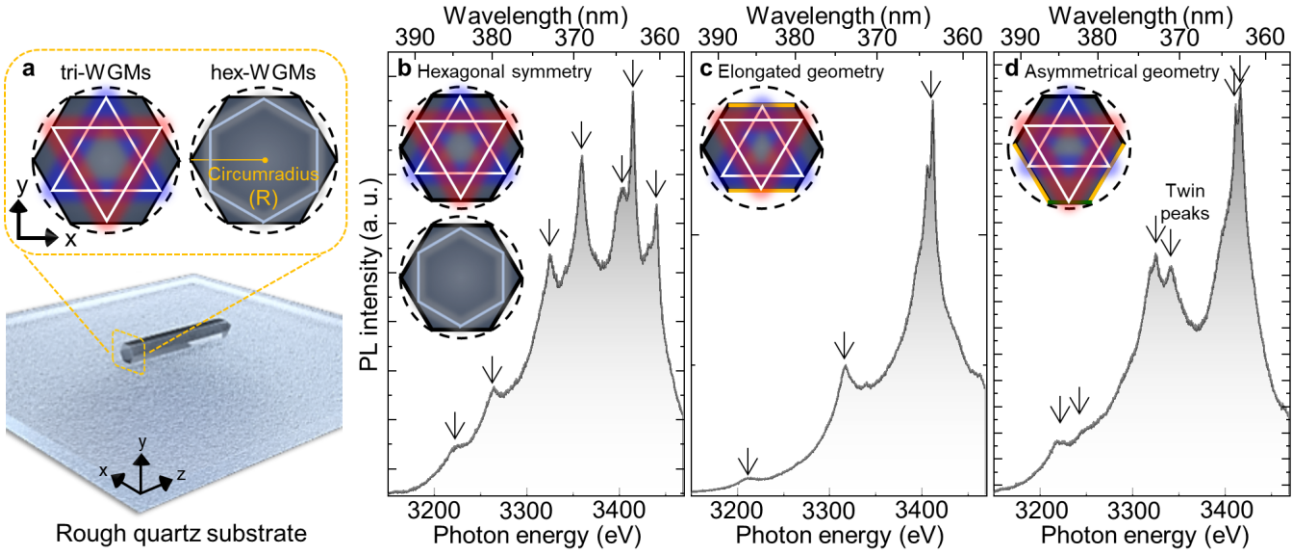

Fig. S1 | Correlation between WGMs and hexagonal geometry. a, Schematics of the hexagonal wire on the rough quartz substrate polished by sandpaper. μPL spectra on the rough quartz substrate (unpatterned substrate) for **b,** Hexagonal symmetry, **c,** Elongated geometry, and **d,** Asymmetry in the hexagonal wire structure.

Section 2. Design of loss-modulated substrate

To design the loss-modulated substrate, we calculated the correlation between the relative position and the simulated loss on the engineered substrate. Fig. S2a represents the optical microscope image of the fabricated loss-modulated substrate. The inset represents the method to design the loss-modulated substrate and how two half ellipses are subtracted from the rectangle. The semi-major axis (a) and semi-minor axis (b) of the ellipse is 4.5 μm and 1.1 μm, respectively, for both the top and bottom part. The dimension of the semi-major and the semi-minor axis is determined by the height and the diameter of the hexagonal wire, respectively. The margin of 300 nm on both the left and right side was intentionally left, considering the spatial resolution of the fabrication. The minimum freestanding width in the center region is corresponding to 300 nm, considering the Rabi splitting energy in our system. The difference between the two ellipses determined the freestanding width as the relative position changed, as shown in Fig. S2b. It is worth noting that this designed substrate provides the adiabatic reduction of the freestanding width to suppress the abrupt degradation of the Q-factor. We interpolated the data of Q-factor for tri↑-WGM and tri↓-WGM (Fig. 2a) in relation to the freestanding width and converted the interpolated data into the photonic loss to be described as $\gamma = \hbar\omega/\mathrm{Q}$. Hence, we can deduce the correlation between the photonic loss and the relative position on the engineered substrate, as shown in Fig. S2c. The blue solid line indicating the loss of tri↑-WGM is negligibly affected by the substrate, while the solid red line corresponding to the loss of tri↓-WGM varies slightly as the relative position changes. Here, the maximum loss, i.e., the region with a minimum freestanding width of 300 nm, is approximately 117 meV, which is lower than the Rabi splitting energy in our system. Therefore, we can maintain the strong coupling regime, i.e., whispering gallery polaritons, under the variation of loss induced by the substrate.

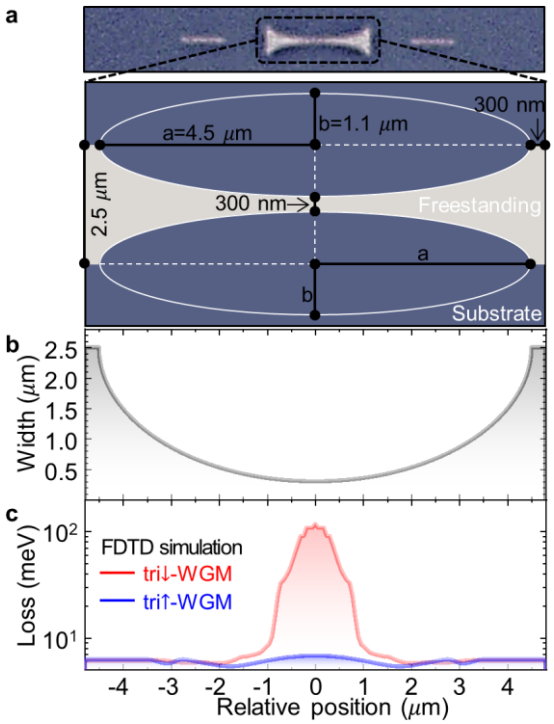

Fig. S2 | Correlation between the relative position and simulated loss on the engineered substrate. a, Optical microscope image of the loss-modulated substrate. (Inset) Designed pattern by the subtraction of two half ellipses. **b,** Freestanding width of the engineered substrate as the relative position changes. **c,** Corresponding photonic loss for the tri↑-WGM and tri↓-WGM concerning the relative position based on interpolated data from FDTD simulation (Fig. 2a).

Section 3. Coupled oscillator Hamiltonian

To identify the exact size of the microcavity, we performed SEM for the microwire that we measured for the experiment as shown in Fig. S3a. We extracted the diameter of the hexagonal microcavity from the difference between two minimum points to exclude the uncertainty of the scaling. Fig. S3b represent the extracted diameter (y-direction) along the wire-axis (x-direction). The result of linear fitting within the loss control substrate region is equal to $y = 1660 - 2.1 \cdot (x - 4)$. Thus, the variation of the circumradius is equal to 830 nm at the bottom and 820 nm at the top.

To calculate our results, we deployed the coupled oscillator Hamiltonian[2] described as

$$\begin{pmatrix} E_X & \hbar\Omega/2 \\ \hbar\Omega/2 & E_C(\theta) \end{pmatrix} \begin{pmatrix} \alpha \\ \beta \end{pmatrix} = E_{pol}(\theta) \begin{pmatrix} \alpha \\ \beta \end{pmatrix},$$

where E_X is the C exciton energy; E_C is the cavity photon energy for the TM mode, and $\hbar\Omega$ is the Rabi splitting energy. For rapid calculation, we implemented a plane-wave model to estimate tri-WGMs and hex-WGMs inside the wire. Here, $E_C(\theta) = E_0/\sqrt{(1 - sin^2\theta/n^2)}$ is the photonic energy-momentum dispersion relation, where $E_0 = (2hc/9nR)\left[N + (3/\pi)\, arctan\left(\sqrt{3n^2 - 4}/n\right)\right]$ and $E_0 = (hc/3\sqrt{3}nR)\left[N + (6/\pi)\, arctan\left(\sqrt{3n^2 - 4}/n\right)\right]$ are the ground cavity photon energies of tri-WGM and hex-WGM[3], respectively, based on the plane-wave model. n is the extraordinary refractive index of GaN; N is the photonic mode number; R is the circumradius of the hexagonal cavity; h is the Planck constant, and c is the speed of light. We assumed that the Rabi splitting energy was independent of the position because the variation of the spatial overlap between photons and excitons was negligible owing to the micro-sized diameter. The parameters used for the calculation were E_X = 3450 meV, n = 3.04, and R = 825 nm and 832 nm for the region at the edge and the center, respectively. The calculated results of $\hbar\Omega$ for tri- and hex-polaritons were 130 ± 7 meV and 130 ± 2 meV, respectively, as shown in Fig. 3b. As our microwire structure was linearly tapered as shown in Fig. S3, we obtained the position-dependent μPL along the z-axis of the same wire on the rough quartz substrate (Fig. S4) to investigate the detuning effect between E_X and E_C. To calculate our results with the coupled oscillator Hamiltonian, we applied the same calculated parameters to the results of angle-resolved μPL except for the circumradius owing to the slightly tapered structure range from the bottom part (R = 830 nm) to the top part (R = 820 nm). Red dashed lines and dotted lines in Fig. S4b represent the calculated dispersions of tri-LP and hex-LP, respectively.

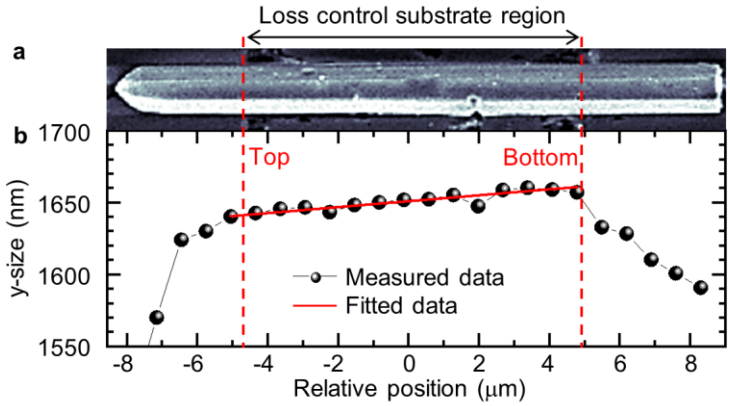

Fig. S3. Variation of the diameter of the hexagonal microcavity depending on the wire-axis. a, SEM image of the measured microwire. **b,** Extracted data of the diameter of the hexagonal microcavity along the wire-axis.

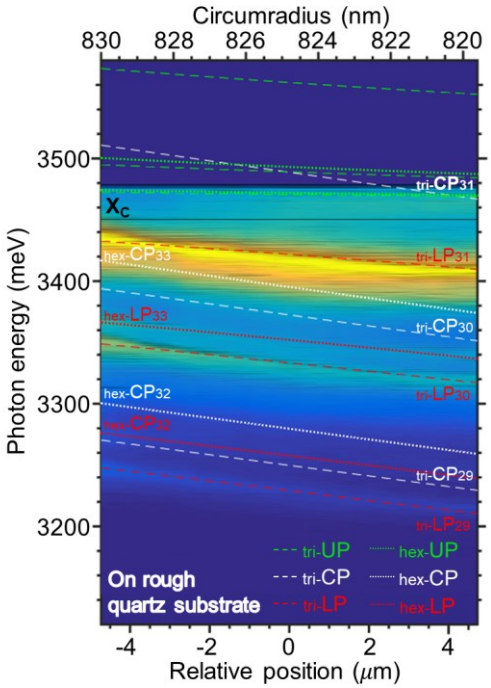

Fig. S4 | Observation of strong coupling on rough quartz substrate. Position-dependent μPL along the z-axis on the rough quartz substrate. Dashed lines for tri-UP, tri-CP, and tri-LP. Dotted lines for hex-UP, hex-CP, and hex-LP.

Section 4. Multiple Lorentzian fitting

To experimentally deduce the strength of direct polariton coupling, μPL spectra are obtained. Fig. S5 shows representative region of μPL spectra at left side (Fig. S4a) in the PT unbroken phase regime, center (Fig. S5b) in the PT broken phase regime, and right side (Fig. S5c) in the PT unbroken phase regime. Red and blue lines indicate the result of multiple fitting based on two Lorentzian profiles. Orange and green lines indicate the result of integrated fitting profiles. In the perspective of peak positions ($\hbar\omega_+$: higher energy side and $\hbar\omega_-$: lower energy side), the fitting result indicate $\hbar\omega_+$=3443.9 ± 0.1 meV and $\hbar\omega_-$=3438.5 ± 0.1 meV (Fig. S5a) as well as $\hbar\omega_+$=3420.2 ± 0.1 meV and $\hbar\omega_-$=3414.5 ± 0.1 meV (Fig. S5c). Thus, experimentally deduced direct polariton coupling strength is about 5.5 meV in the PT unbroken phase. Here, two Lorentzian profiles are degenerated in PT broken phase as shown in Fig. S5b. In the perspective of linewidth (Γ_+ : higher energy side and Γ_- : lower energy side), the fitting result indicate Γ_+=3.0 ± 0.1 meV and Γ_-=7.5 ± 0.4 meV (Fig. S5a) as well as Γ_+= 3.0 ± 0.1 meV and Γ_- =6.9 ± 0.2 meV (Fig. S5c) in the PT unbroken phase. The results of Γ_+ for both are narrower than those of Γ_-. The results of Γ_- are close to the linewidth of PT broken phase ($\Gamma_\pm$=7.0 ± 0.1 meV)

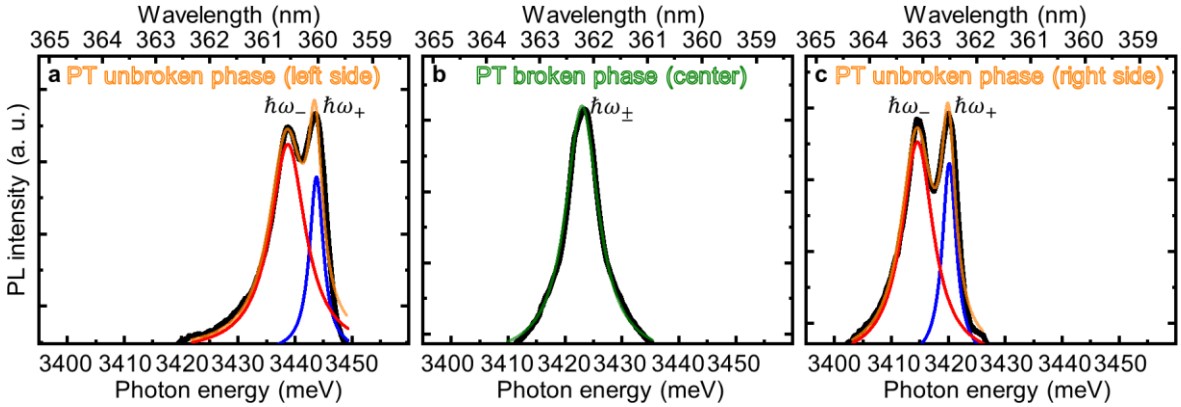

Fig. S5 | Multiple Lorentzian fitting for the direct observation of polariton coupling. μPL spectra are shown at **a,** Left side, i.e., higher energy side, in the regime of PT unbroken symmetry, **b,** Center, i.e., strong loss region, in the regime of PT broken symmetry, and **c,** Right side, i.e., lower energy side, in the regime of PT unbroken symmetry. Red and blue lines indicate the result of multiple fitting based on two Lorentzian profiles. Orange and green lines indicate the result of integrated fitting results

Section 5. Comparison of polariton condensate threshold on the rough quartz substrate and the loss-modulated substrate

As the excitation power density increases, we could obtain the polariton condensate in a rather wider range of distance at the right (bottom, positive position) region compared to at the left (top, negative position) region on the loss-modulated substrate as well as on the rough quartz substrate, as explained below. Our wire structure shows positively detuning ($\Delta=E_{tri\text{-}CP31}-E_{Xc}$) extracted from Fig. S4 and the value of detuning increases from the right (bottom) to the left (top) side as shown in Fig. S6a. For reference, Fig. s6b show the threshold of polariton condensate as a function of relative position when the structure is on the rough quartz substrate (i.e., before PDMS stamp transfer). We found a slight and gradual increase in the threshold from the right to the left with an increment of detuning value[4-6] (see [†]**Polariton condensate threshold as a function of detuning** for details as below). We note that the optical pumping experiments especially at room temperature should be carried out with extra caution during the whole experiments not to damage a single wire structure on a freestanding substrate which has poorer heat dissipation. Hence, we tried to acquire more excitation power dependent data in the right (bottom) side with slightly lower threshold, over the wider range of distance (compared to the left (top) side) for clarifying phase transition. Fig. s6c represents the threshold of polariton condensate as a function of relative position on the loss-modulated substrate, i.e., after

[†]**Polariton condensate threshold as a function of detuning**.

Polariton condensate threshold is mainly determined by the polariton-polariton scattering rate to reach the ground state within the limited polariton lifetime. As the interaction is in charge of exciton, this polariton-polariton scattering rate is determined by the excitonic fraction. Here, larger detuning value results in higher excitonic fraction. Hence, the threshold of polariton condensate is reduced as the lower polariton energy level is close to the exciton energy level in ideal case, i.e. without consideration of exciton-phonon scattering. However, the effect of polariton-phonon scattering cannot be negligible in the practical semiconductor system. As a result, as the excitonic fraction increases (i.e., for larger value of detuning), polariton-phonon scattering rate also increases and competes with the polariton-polariton scattering. Hence, the effective polariton-polariton scattering is reduced and this contribute to increase the threshold[4-6]. Since the detuning value in our system is located in dominant polariton-phonon scattering regime (thermodynamic regime), the threshold gradually increases as the value of detuning increases.

PDMS stamp transfer. Furthermore, to exclude the detuning effect, we extracted the ratio of the threshold before and after PDMS transfer as shown in Fig. S6d. Both Fig. S6c and Fig. S6d clearly exhibit that the threshold ratio decreases from the right (PT unbroken phase) to the center (PT broken phase) first, and then increases again from the center (PT broken phase) to the left (PT unbroken phase) due to the bifurcation of imaginary eigenvalues in non-Hermitian degeneracies. We note that this decreasing tendency of the threshold from the both ends (left and right) to the center on the loss-modulated substrate provides the clear evidence of the counterintuitive effect reversing loss into gain in non-Hermitian system.

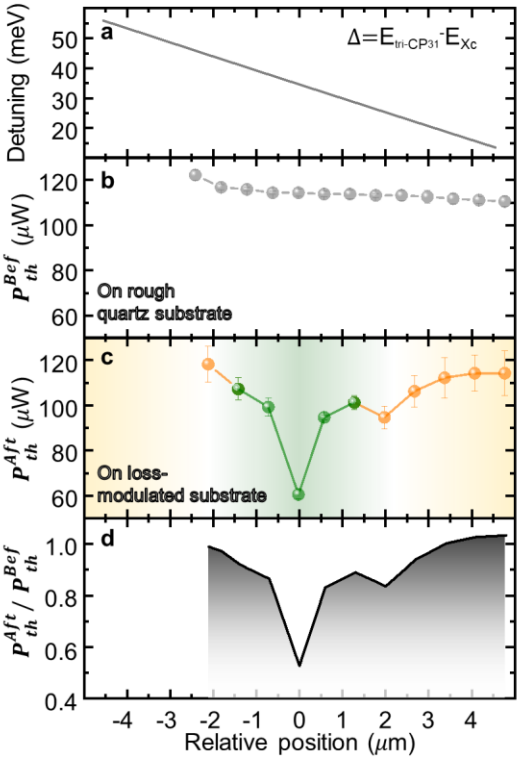

Fig. S6 | Comparision of polariton condensate threshold on the rough quartz substrate and the loss-modulated substrate. **a,** Extracted detuning between tri-CP31 and E_{Xc} in relation to the relative position of the wire structure. Threshold of polariton condensate as a function of the relative position **b,** on the rough quartz substrate, and **c,** on the loss controlled substrate. **d,** Ratio of the threshold before and after PDMS transfer.

Section 6. Coupled polariton Hamiltonian

To analyse the experimental data in Fig. 5b, we modelled the coupled polariton Hamiltonian with gain and loss as follows:

$$\begin{pmatrix} E_{X_\uparrow} & \hbar\Omega_\uparrow/2 & 0 & \hbar g \\ \hbar\Omega_\uparrow/2 & E_{C_\uparrow} + i\hbar\gamma_\uparrow - i\hbar p_\uparrow & \hbar g & 0 \\ 0 & \hbar g & E_{X_\downarrow} & \hbar\Omega_\downarrow/2 \\ \hbar g & 0 & \hbar\Omega_\downarrow/2 & E_{C_\downarrow} + i\hbar\gamma_\downarrow - i\hbar p_\downarrow \end{pmatrix} \begin{pmatrix} \alpha \\ \beta \\ \gamma \\ \delta \end{pmatrix} = E_{pol}(\theta) \begin{pmatrix} \alpha \\ \beta \\ \gamma \\ \delta \end{pmatrix}.$$

For the calculation, the value of Rabi splitting energy ($\hbar\Omega$) of tri↑-polariton and tri↓-polariton is first deduced by the coupled oscillator Hamiltonian from the result of angle-resolved μPL (Fig. 3b). As the value of cavity photon energy (E_c) of tri↑-polariton and tri↓-polariton is identical on account of the hexagonal symmetry, it is deduced by coupled oscillator Hamiltonian from the result of position-dependent μPL (Fig. S4) based on the result of SEM image (Fig. S3) to consider the linearly tapered geometry. The value of polariton coupling energy ($\hbar g$) between tri↑-polariton and tri↓-polariton is determined by the result of the direct observation in the freestanding region, i.e., the region with the widest freestanding width (Fig. 3e). The value of photonic loss by the tailored substrate for tri↑-polariton and tri↓-polariton is ascertained by the simulated result of FDTD (Fig. 3f). As the value of the excitonic loss is approximately three orders lower than that of photonic loss, it is negligible. Hence, solely the gain terms ($\hbar p$) of the optical pump are fitting parameters; the other terms are predetermined by angle-resolved μPL, position-dependent μPL, and FDTD simulations. Table S1 represents the parameters for the calculation of the coupled polariton Hamiltonian considering gain and loss.

	tri↑-polariton	tri↓-polariton
Exciton energy	$E_{X_\uparrow}$=$E_{X_\downarrow}$=3450 meV	
Cavity photon	$E_{C_\uparrow}$=$E_{C_\downarrow}$: from 3405 meV to 3412.5 meV	
Vacuum Rabi splitting	$\hbar\Omega_\uparrow$=$\hbar\Omega_\downarrow$= 130 meV	
Polariton coupling	$\hbar g$=2.75 meV	
Loss	Refer to Fig. 3e	
Gain	16 meV	8 meV

Table S1 | Parameters for the calculation of coupled polariton Hamiltonian considering gains and losses

Section 7. Energy-momentum dispersion of the one-dimensional microcavity

To observe the behaviour of polariton condensate for all three regimes, we conducted angle-resolved μPL along the detection angle θ_z, in contrast to the Fig. 5d data taken along the detection angle θ_x (confined plane). Fig. S7 a-c represent the energy-momentum dispersion above the threshold for three regimes, a, PT broken phase, b, Exceptional point, and c, PT unbroken phase. (In PT unbroken phase, intensity of lower energy side is multiplied by factor 3 times for clarity.) The dispersion data along the angle θ_z (Fig. S7) represent the massive emission from around $\theta_z = 0$, while the dispersion along the angle θ_x (Fig. 5d) showed the flat dispersion with the interference pattern above the threshold. These behaviours are attributed to the unique properties of one-dimensional microcavity. In other words, the wave vectors in radial plane (x-y plane) are confined within the cross-section of the wire.

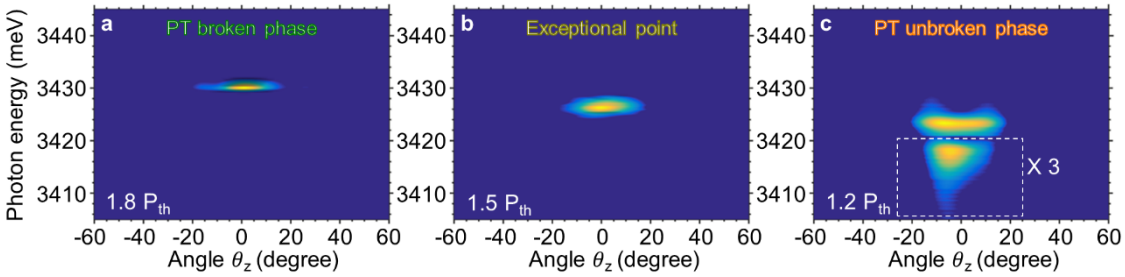

Fig. S7 | Energy-momentum dispersion above the threshold for three regimes. Energy-momentum dispersion along the detection angle θ_z at **a**, PT broken phase, **b**, Exceptional point, and **c**, PT unbroken phase. In PT unbroken phase, intensity of lower energy side is multiplied by 3 times for clarity.

References

1 Wiersig, J. Hexagonal dielectric resonators and microcrystal lasers. *Phys. Rev. A* **67** (2003).

2 Gong, S.-H., Ko, S.-M., Jang, M.-H. & Cho, Y.-H. Giant rabi splitting of whispering gallery polaritons in GaN/InGaN core–shell wire. *Nano Lett.* **15**, 4517-4524 (2015).

3 Sun, L. *et al.* Quasi-whispering gallery modes of exciton-polaritons in a ZnO microrod. *Opt. Expres.* **18**, 15371-15376 (2010).

4 Butte, R. et al. Phase diagram of a polariotn laser from cryogenic to room temperature. *Phy. Rev. B* **80**, 233301 (2009)

5 Georg, R. et al, Impact of saturation on the poalrization renormalization in III-nitride bsed planar microcavities. *Phy. Rev. B* **88**, 165312 (2013)

6 Jamadi, O. et al, Polariton condensation phase diagram in wide-band-gap planar microcavities : GaN versus ZnO. *Phy. Rev. B* **93**, 115205 (2016)